The first principles investigation of ferrite magnetic response with mismatch stress

HUANG JunPing[1,3*], PENG XiangHe[1] & HU XianZhi[2]

[1] *Department of Engineering Mechanics, Chongqing University, Chongqing 400044, China;*
[2] *Faculty of Science, Kunming University of Science and Technology, Kunming 650093, China;*
[3] *School of Mechanical Engineering, Chongqing Vocational Institute of Engineering, Chongqing 400037, China*

The quasi-ferrite model is proposed and an appropriate PBE exchange functional with the spin density functional theory (SDFT) is selected for the calculation of the relation between magnetic moment and residual stress in ferrite using a quantum mechanics code. The relationship between ferrite magnetism and the carbon content is determined, and then a ferrite interstitial solid solution (ISS) model in a low carbon concentration state is replaced with an α-Fe model in the case of majority magnetic calculation. The band structure of the loaded α-Fe is compared with that of the unloaded α-Fe. The comparison shows that the energy of Fe atomic 3d orbital changes a little, while the energy of electron orbital of iron core below 3d almost keeps unchanged. The relationship between the magnetic moment and the stress appears intermittent due to the Bragg total reflection. The change in the magnetic moment due to lattice mismatch is much larger than that caused by mechanical loading.

1 Introduction

The non-destructive testing (NDT) techniques based on metal magnetic memory (MMM) principle were used to detect defects in the stress concentration zone of ferromagnetic materials at the beginning of the 1980s by the Russian researcher Doubov [1–3]. At the same time, the researchers made great efforts to establish the material constitutive model at the level of macroscale [4–6] because of important applications of this kind of function materials，such as in these scopes of sonar, brakes, dampers, smart filters, high power motors, robotics, and noise and vibration control. In essence, MMM is one of the characteristic performances of magnetostrictive materials. On the one hand，there is still lack of systematic test data for researchers' investigation of the coupling relationship between the stray field signals and stress, for they focus mainly on the combined meso-macroscopic studies of characterized law of fatigue crack initiation, evolution and fatigue damage assessment currently, although MMM theory and techniques used in the study of the fatigue damage had some basic results. In fact, the coupling relationship is very complex. If the response can be clarified to a certain extent, it is possible to determine signal variation rules of early damage of ferromagnetic component. On the other hand, there is hardly any researcher engaged in studying the magnetic memory mechanism induced by vacancy defects and doping on the atomic scale. The variation of the magnetic property of ferrous metals due to the residual stress induced by lattice mismatch

---

*Corresponding author (email: jphuang_63@163.com)

is very important as research subjects. The purpose of this paper, using quasi-ferrite and appropriate selected density functional as the temperature-independent computational model, is to investigate the relationship between magnetic changes and lattice mismatch by the first-principles methods, and do fundamental work for temperature-dependent computational model research subsequently such as the molecular dynamic models and microscopic constitutive relations.

2 Spin Density Functional Theory (SDFT) and calculation model

2.1 SDFT

Barth and Hedin [7] as well as Pant and Rajagopal [8] proposed the SDFT separately. Though it is the same method as the density functional theory (DFT) establishment, SDFT differs in the extra magnetic interaction term in the potential function in addition to electrostatic interactions. Thus, the Hamiltonian operator for the system is

$$\hat{H} = -\frac{1}{2}\sum_{i=1}^{N}\nabla_i^2 + \sum_{i<j}^{N}\sum \frac{1}{r_{ij}} + \sum_{i=1}^{N}V(r_i) + 2\mu_B\sum_{i=1}^{N}\boldsymbol{B}(r)\cdot\boldsymbol{s}_i, \quad (1)$$

where $\mu_B = e\hbar/2m_e$ is the Bohr magneton; $\hbar = h/2\pi$, h is the Planck's constant; e is the electronic charge; m_e is the electron rest mass; r_{ij} is the distance between the interact electrons of ith and jth; $V(r_i)$ is the electrostatic potential function; r_i is the position vector of ith electron; $\boldsymbol{B}(r)$ is magnetic flux density, and $\boldsymbol{s}_i$ is the spin angular momentum of the ith electron, respectively. Thus the third and fourth terms on the RHS of eq. (1) can be combined as an external potential term

$$\hat{V} = \sum_{i=1}^{N}V(r_i) + 2\mu_B\sum_{i=1}^{N}\boldsymbol{B}(r)\cdot\boldsymbol{s}_i$$
$$= \int V(r)\hat{\boldsymbol{\rho}}(r)\cdot dr + \int \boldsymbol{B}(r)\cdot\hat{\boldsymbol{m}}(r)dr, \quad (2)$$

where $\hat{\boldsymbol{\rho}}(r) = \sum_{i=1}^{N}\delta(r-r_i)$ is the operator of electron density, $\hat{\boldsymbol{m}}(r) = -2\mu_B\sum_{i=1}^{N}\boldsymbol{s}_i\delta(r-r_i)$ is the electronic magnetization operator. If $\boldsymbol{B}(r)$ and $\hat{\boldsymbol{m}}(r)$ have the same direction, the expectation of $\hat{V}$ is

$$\langle\Psi|\hat{V}|\Psi\rangle = \int V(r)\rho(r)\cdot dr - \int \boldsymbol{B}(r)\cdot\boldsymbol{m}(r)dr$$
$$= \int V(r)\rho(r)dr - \int B(r)m(r)dr, \quad (3)$$

where

$$\rho(r) = \langle\Psi|\hat{\boldsymbol{\rho}}(r)|\Psi\rangle = \langle\Psi|\sum_{i=1}^{N}\delta(r-r_i)|\Psi\rangle$$
$$= \rho_\alpha(r) + \rho_\beta(r), \quad (4)$$

$$m(r) = -2\mu_B\langle\Psi|\sum_{i=1}^{N}s_i\delta(r-r_i)|\Psi\rangle$$
$$= -2\mu_B\sum_{s=\alpha,\beta}s_i\rho_s(r)$$
$$= -2\mu_B\left[\frac{1}{2}\rho_\alpha(r) - \frac{1}{2}\rho_\beta(r)\right]$$
$$= -\mu_B\left[\rho_\alpha(r) - \rho_\beta(r)\right]. \quad (5)$$

$\rho_\alpha(r)$ and $\rho_\beta(r)$ are the electron density of spin states α and β, respectively. According to the constraint search method proposed by Levy [9], the ground state energy is

$$E_0 = \inf_\Psi \langle\Psi|\hat{\boldsymbol{T}} + \hat{\boldsymbol{V}}_{ee} + \sum_{i=1}^{N}V(r_i) + 2\mu_B\sum_{i=1}^{N}\boldsymbol{B}(r_i)\cdot\boldsymbol{s}_i|\Psi\rangle$$
$$= \inf_{\rho_\alpha,\rho_\beta}\left\{\inf_{\Psi\to\rho_\alpha,\rho_\beta}\langle\Psi|\hat{\boldsymbol{T}}+\hat{\boldsymbol{V}}_{ee}|\Psi\rangle + \int[V(r)\rho(r) - B(r)m(r)]dr\right\}$$
$$= \inf_{\rho_\alpha,\rho_\beta}\Big\{F\left[\rho_\alpha,\rho_\beta\right]$$
$$+ \int\left[\big(V(r)+\mu_B B(r)\big)\rho_\alpha(r) + \big(V(r)-\mu_B B(r)\big)\rho_\beta(r)\right]dr\Big\}$$
$$= \inf_\rho E\left[\rho_\alpha,\rho_\beta\right], \quad (6)$$

where $F\left[\rho_\alpha,\rho_\beta\right] = \inf_{\Psi\to\rho_\alpha,\rho_\beta}\langle\Psi|\hat{\boldsymbol{T}}+\hat{\boldsymbol{V}}_{ee}|\Psi\rangle$. Suppose the spin-orbital functions $\{\phi_{i\sigma},\sigma=\alpha,\beta\}$ satisfy the condition of $\sum_i n_{i\alpha}|\phi_{i\alpha}(r)|^2 = \rho_\alpha(r)$ and $\sum_i n_{i\beta}|\phi_{i\beta}(r)|^2 = \rho_\beta(r)$, $n_{i\sigma}(\sigma=\alpha,\beta)$ are the spin numbers, the total energy can be expressed as the functional of $\{\phi_{i\sigma},\sigma=\alpha,\beta\}$ as:

$$E\left[\rho_\alpha,\rho_\beta\right] = \sum_{i,\sigma}n_{i\sigma}\int dr\phi_{i\sigma}^*(r)\left(-\frac{1}{2}\nabla^2\right)\phi_{i\sigma}(r)$$
$$+ J\left[\rho_\alpha+\rho_\beta\right] + E_{XC}\left[\rho_\alpha,\rho_\beta\right]$$
$$+ \int dr\left\{[V(r)+\mu_B B(r)]\rho_\alpha(r)\right.$$
$$\left. + [V(r)-\mu_B B(r)]\rho_\beta(r)\right\}, \quad (7)$$

where $E_{XC}\left[\rho_\alpha,\rho_\beta\right]$ is the exchange-correlation energy, $J\left[\rho_\alpha+\rho_\beta\right]$ is the classical Coulomb energy. Under the condition that $\{\phi_{i\sigma},\sigma=\alpha,\beta\}$ satisfies the constraints of orthonormality, one takes the variation of $E\left[\rho_\alpha,\rho_\beta\right]$ with respect to $\phi_{i\sigma}$ and extremum value, and then gets Kohn-Sham equation of SDFT

$$\hat{H}_{\text{eff}}^{\sigma}\phi_{i\sigma}(\boldsymbol{r}) = \left[-\frac{1}{2}\nabla^2 + V_{\text{eff}}^{\sigma}\right]\phi_{i\sigma}(\boldsymbol{r})$$

$$= \frac{\varepsilon_{i\sigma}'}{n_{i\sigma}}\phi_{i\sigma}(\boldsymbol{r}) \equiv \varepsilon_{i\sigma}\phi_{i\sigma}(\boldsymbol{r}), \qquad (8)$$

$$\sigma = \alpha, \beta,$$

where $\varepsilon_{i\sigma}'$ are Lagrangian multipliers,

$$V_{\text{eff}}^{\alpha}(\boldsymbol{r}) = V(\boldsymbol{r}) + \mu_{\text{B}}B(\boldsymbol{r}) + \int\frac{\rho(\boldsymbol{r}')}{|\boldsymbol{r}-\boldsymbol{r}'|}\mathrm{d}\boldsymbol{r}' + \frac{\delta E_{\text{XC}}[\rho_{\alpha},\rho_{\beta}]}{\delta\rho_{\alpha}}; \quad (9)$$

$$V_{\text{eff}}^{\beta}(\boldsymbol{r}) = V(\boldsymbol{r}) - \mu_{\text{B}}B(\boldsymbol{r}) + \int\frac{\rho(\boldsymbol{r}')}{|\boldsymbol{r}-\boldsymbol{r}'|}\mathrm{d}\boldsymbol{r}' + \frac{\delta E_{\text{XC}}[\rho_{\alpha},\rho_{\beta}]}{\delta\rho_{\beta}}, \quad (10)$$

and $\int\rho_{\alpha}(\boldsymbol{r})\mathrm{d}\boldsymbol{r} = N_{\alpha}$, $\int\rho_{\beta}(\boldsymbol{r})\mathrm{d}\boldsymbol{r} = N_{\beta}$, $N_{\alpha} + N_{\beta} = N$, N_{α} and N_{β} are the numbers of electrons with the spin states α and β.

2.2 The selection of density functional

The local spin density approximation (LSDA) functional is built on an ideal model based on the homogeneous electron gas, while the actual electron density of atomic or molecular system is far from homogeneous, and thus, the calculated results by the LSDA are usually not similar to the physical and chemical natures of materials actually. In order to make the analysis more accurate, the inhomogeneity of the electron density should be considered by introducing the electron density gradient in the exchange-correlation energy functional, which leads to a generalized gradient approximation (GGA) functional.

Many GGA-type exchange energy functional expressions have been proposed, such as the Becke's [10] plus gradient corrected exchange energy functional B88, the Perdew and Wang's [11,12] exchange energy functional PW91, and the Perdew, Burke and Ernzerhof's [13] exchange energy functional PBE, etc.

PBE is improved based on PW91 and can be expressed as:

$$E_{\text{XC}}^{\text{PBE}}[\rho_{\sigma}, x_{\sigma}] = E_{\text{X}}^{\text{PBE}}[\rho_{\sigma}, x_{\sigma}] + E_{\text{C}}^{\text{PBE}}[\rho_{\sigma}, \varsigma], \qquad (11)$$

$$E_{\text{X}}^{\text{PBE}}[\rho_{\sigma}, x_{\sigma}] = E_{\text{X}}^{\text{LSDA}}[\rho_{\sigma}]$$

$$- C_{\text{X}}\int a\left(1 - \frac{1}{1+bx_{\sigma}^2}\right)\rho_{\sigma}^{4/3}\boldsymbol{r}\cdot\mathrm{d}\boldsymbol{r}, \qquad (12)$$

$$E_{\text{C}}^{\text{PBE}}[\rho_{\sigma}, \varsigma] = E_{\text{C}}^{\text{LSDA}}[\rho_{\sigma}, \varsigma] + \int G[t(\boldsymbol{r})]\rho(\boldsymbol{r})\cdot\mathrm{d}\boldsymbol{r}, \qquad (13)$$

where E_{X} is the exchange energy functional, and $x_{\sigma}(\sigma = \alpha, \beta)$ is the dimensionless reducible density gradient (RDG), i.e., $x_{\sigma} = |\nabla\rho_{\sigma}|\rho_{\sigma}^{3/4}$, $C_{\text{X}} = \frac{3}{4}\left(\frac{3}{\pi}\right)^{1/3}$, $a = 0.804$

and $b = 0.273$ are non-empirical parameters based on the physical conditions; E_{C} is the correlation energy functional,

$$G[t(\boldsymbol{r})] = cf^3(\varsigma)\ln[1 + (1+Bt^2(\boldsymbol{r}))/(1 + Bt^2(\boldsymbol{r}) + B^2t^4(\boldsymbol{r}))],$$

$$B = g[\exp(-\varepsilon_{\text{C}}^{\text{LSDA}}/cf^3(\varsigma)) - 1]^{-1},$$

$$t(\boldsymbol{r}) = |\nabla\rho(\boldsymbol{r})|/2f(\varsigma)k_{\text{s}}\rho(\boldsymbol{r}),$$

$$f(\varsigma) = \left[(1+\varsigma)^{2/3} + (1-\varsigma)^{2/3}\right]/2, \quad k_{\text{s}} = \left[4(3\pi^{-1}\rho(\boldsymbol{r}))^{1/3}\right]^{1/2},$$

ς is the spin polarization, ε_{C} is the correlation energy of a single electron, $c = 0.031091$ and $g = 2.146119$ are also non-empirical parameters based on the physical conditions [13]. Therefore, the PBE will be selected in the following calculation.

2.3 The structural model and calculation method

Based on SDFT, the magnetic properties and the mismatch stress of ferrite have been calculated using the functional PBE of GGA. Since the carbon concentration of the calculated ferrite is very extremely low (about 0.0008% at room temperature), it is obviously hard to calculate these models which have much more atoms in super cells using quantum mechanics codes because the number of the atoms involved hardly exceeds 100. In getting rid of this obstacle, the quasi-ferrite model is proposed firstly, with which the enabled model is close to 1.00% of carbon concentration, so that the constrained and non-constrained α-Fe interstitial solid solution (ISS) super-lattice model can be calculated, and the effect of the lattice mismatch on the structure and the magnetic property can be determined. At the same time, it is easier to calculate the response of pure iron single crystals between the mismatch stress and magnetism by extrapolation, and obtain the relationship between the carbon concentration and the magnetism of ferrite. With these results, we conclude that the low concentrated carbon ferrite can completely be substituted by pure iron crystal, so that the body-centered cubic lattice of pure iron single crystal can be used for the model calculation in the case of the [111] direction loaded and considering the lattice mismatch.

The calculation of this work is completed by the code of Vienna *Ab-initio* Simulation Package (VASP). Based on SDFT and the pseudopotential plane wave method, geometric optimization is realized by the expansion of plane wave basis, and the exchange-correlation function takes the form of PBE in the GGA. The details of a particular pseudopotential define a minimum energy cutoff that should be used in our calculations including atoms associated with that pseudopotential. Pseudopotentials requiring high cutoff energies are said to be hard, while more computationally efficient pseudopotentials with low cutoff energies are soft. The most widely used method of defining pseudopotentials in this paper is based on the work by Vanderbilt; these are the ultrasoft pseudopotentials (USPPs). As their name suggests,

these pseudopotentials require substantially lower cutoff energies than alternative approaches. The energy cutoff is 280 eV, which is a default parameter after the model built. In accordance with the sampling of the Brillouin zone (BZ) Monkhorst-Pack k point method, the suite k points are selected automatically to ensure the higher convergence precision. Table 1 shows the MP grid size for SCF calculations and the number of k points used corresponding to the super cells. The total energy convergence tolerance is 2.0×10^{-5} eV/atom, and the maximum of stress component tolerance is 0.1 GPa .

The calculation process contains three steps: (1) Periodic or non-periodic super cells are constructed according to model requirement; (2) the geometry of the models is optimized, including the minimization of electronic energy of the system and the stabilization of the geometry structure; (3) the other properties are calculated, such as the relations between the magnetic nature and the mismatch of the structure.

Because the same unchanged lattice constants along with (100) and (001) directions in super cells are $1 \times \underset{n \to \infty}{n} \times 1$, and while the lattice constant in the direction of (010) is an integer times value of a or c , it is not surprising that the k points in reciprocal space is default selected as $7 \times M \times 7k$ points. The last two columns in Table 2 list the computational total energy per atom and the energy difference between the symmetric $7 \times 7 \times 7$ and $7 \times 1 \times 7k$ points. It can be seen from Table 2 for the smaller super cells ($n \leq 6$) that the better convergence can be obtained due to the relatively smaller values of energy difference between the symmetric $7 \times 7 \times 7$ and $7 \times 1 \times 7k$ points, while $n \geq 8$ the energy difference ΔE has significantly increased. This indicates that fitted curve by these calculated results could not be smooth. However, the minor energy difference in the acceptable range indicates that the computational results are still reliable.

3 Results and discussion

3.1 The effect of carbon concentration on the magnetic properties in ferrite

Ferrite is an ISS formed by C atoms dissolved in the iron cells. Because a C atom forms Fe-C metal compounds with its neighboring Fe atoms, it will affect the 3d orbital electron's spin state of the Fe atoms, which in turn changes its magnetic moment. In the calculation, the carbon concentration of the quasi-ferrite model is directly related to the number of atoms, so a higher carbon concentration should correspond to a smaller lattice state, which is definitely different from the actual ferrite. Therefore, it is nearly impossible for the first-principle calculation codes to build a low carbon concentration model for ferrite. In order to eliminate the effect of crystal periodic impact of the cell, the group number 1P1 is put in, so the concentration of C atoms is calculated with the total atoms in a unit cell. Figure 1(a) shows the shape of $1 \times 2 \times 1$ super lattice-like quasi-ferrite unit cell model corresponding to the C concentration of 6.67%, while the shape of $1 \times 4 \times 1$ unit cell (Figure 1 (b)) corresponds to 4.00% of C concentration. Such a high concentration is far from that of ferrite at room temperature state. That the first-principles code can calculate about 1.00% C concentration model in principle is conventional calculation. The band structure diagram shows that the electronic structure of the super lattice-like quasi-ferrite is the majority of C $2s^2 2p^2$ and Fe $3d^6 4s^2$ level electrons.

Table 3 is the Mullikan population analysis of the $1 \times 2 \times 1$ super lattice-like quasi-ferrite, and Table 4 is interaction

Figure 1 (Color online) High carbon concentrations of the quasi-ferrite model. (a) $1 \times 2 \times 1$ super lattice-like quasi-ferrite; (b) $1 \times 4 \times 1$ super lattice-like quasi-ferrite.

Table 1 MP grid size for SCF calculations and the number of k points

Number of cells	MP grid size for SCF	number of k points
$1 \times 2 \times 1$	$7 \times 3 \times 7$	74
$1 \times 4 \times 1$	$7 \times 2 \times 7$	49
$1 \times 6 \times 1$	$7 \times 1 \times 7$	25
$1 \times 8 \times 1$	$7 \times 1 \times 7$	25
$1 \times 10 \times 1$	$7 \times 1 \times 7$	25
$1 \times 12 \times 1$	$7 \times 1 \times 7$	25

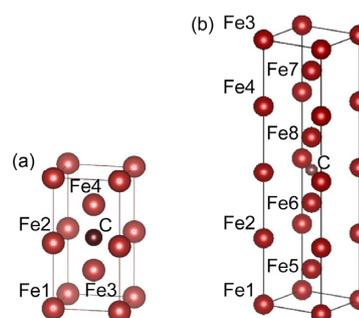**Table 2** Total energy and the energy difference

Number of cells	MP grid size for SCF	Number of k points in BZ	Total energy E/atom (eV)	Energy difference between the symmetric $7 \times 7 \times 7k$ points and $7 \times 1 \times 7k$ points ΔE/atom (eV)
$1 \times 2 \times 1$	$7 \times 3 \times 7$	74	−903.38381750	−0.00044250
$1 \times 4 \times 1$	$7 \times 2 \times 7$	49	−884.19710750	−0.00058750
$1 \times 6 \times 1$	$7 \times 1 \times 7$	25	−877.81534167	−0.00054583
$1 \times 8 \times 1$	$7 \times 1 \times 7$	25	−874.58736875	−0.00687832
$1 \times 10 \times 1$	$7 \times 1 \times 7$	25	−872.65345500	−0.00732541
$1 \times 12 \times 1$	$7 \times 1 \times 7$	25	−871.38618333	−0.00698256

Table 3   1×2×1 Super lattice-like quasi-ferrite Mullikan population analysis

Species	s	p	d	f	Total	Charge (e)	Spin (ħ)
C1	1.50	3.21	0.00	0.00	4.71	−0.71	−0.13
Fe1	0.69	0.64	6.58	0.00	7.91	0.09	1.28
Fe2	0.31	0.48	6.75	0.00	7.54	0.46	0.82
Fe3	0.54	0.71	6.66	0.00	7.92	0.08	1.04
Fe4	0.54	0.71	6.67	0.00	7.92	0.08	1.03

Table 4   Interaction length distribution of 1×2×1 super lattice-like quasi-ferrite

Interaction	Population	Spin	Length (Å)
C1-Fe4	0.14	0.04	1.86211
C1-Fe3	0.14	0.04	1.86213
C1-Fe2	1.58	−0.03	1.90677
Fe1-Fe4	0.29	0.04	2.46386
Fe1-Fe3	0.29	0.04	2.46387
Fe2-Fe3	−0.04	−0.03	2.66518
Fe2-Fe4	−0.04	−0.03	2.66521

length distribution of the 1×2×1 super lattice-like quasi-ferrite. Table 1 shows that the atom Fe1 is furthest away from the C atom and less affected by the C atom, so the magnetic moment is the largest, $2.56\mu_B$. However, it bears no evidence that the magnetic moment of the Fe atom within the influence of the adjacent C atom fully depends on the distance of the two atoms, because the main factors determining the magnetic moment of the Fe atom is the unpaired electron spin state of 3d energy level. It can be seen in Table 3 that the electron charge distribution in orbital 3d of Fe2 atom is significantly greater than that of Fe3 and Fe4 despite being far away from the C atom. It is clear in Figure 1(b) that the concentration of C atom decreases with the increase of the atomic layer. The magnetic moment of atom Fe4 is $1.38\mu_B$, and the corresponding interaction length of Fe-C between Fe4 and C is 1.84643 Å. Similarly, the magnetic moments of Fe6 and Fe7 are $1.96\mu_B$, and the corresponding Fe-C interaction length is 1.9029 Å. Since the moment of α-Fe at zero carbon concentration is known, it is possible to find out approximately the relationship of the quasi-ferrite between the magnetic nature and the carbon concentration, and to determine the response of low carbon

quasi-ferrite close to the reality. Table 5 is the variant of magnetic moment for the different cells in direction (010), i.e., the average magnetism change of atoms in the cell with the carbon concentration decreases. The magnetic calculation of the $1 \times n \times 1 \atop n \to \infty$ near-ferrite is equivalent to the calculation of the 1×1×1 α-Fe ferrite.

Figure 2 shows the fitting curve for the response of the magnetism and the carbon concentration. Since the C concentration falls from 2.222% to zero, the change of magnetic moment is only about 1.567%. It can be seen that the following cubic polynomial fit relationship could reasonably approximate the response if the C concentration is less than 1.567%

$$\bar{M} = 2.23942 - 0.07399\hat{C} + 0.01658\hat{C}^2 - 0.00155\hat{C}^3, \quad (14)$$

where $\bar{M}$ is the average magnetic moment of atoms, and $\hat{C}$ is the concentration percentage of the C atom. Supposing the terms in eq. (14), of which the orders are equal to or higher than the square, were omitted, then the response of eq. (14) would degenerate to linear equation just as the C concentration tends to be 0.0008%.

Table 5   Magnetism of quasi-ferrite and C concentration

Number of cells	Number of atoms	Concentration of C (%)	2×Integrated spin density (ħ)	Average magnetism of atoms (μ_B)
1×2×1	15	6.667	8.09485	2.0237
1×4×1	25	4.000	16.9136	2.1142
1×6×1	35	2.857	25.4263	2.1189
1×8×1	45	2.222	34.5223	2.1576
1×10×1	55	1.818	42.7396	2.1369
1×12×1	65	1.538	51.8512	2.1605
$1 \times n \times 1 \atop n \to \infty$ (α-Fe)	∞	0.000	8.7677	2.2384
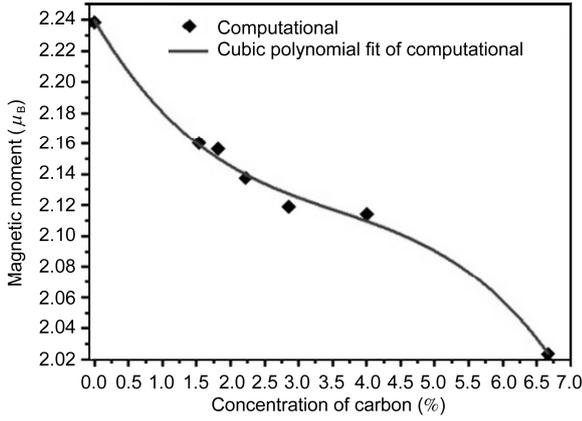
Figure 2   Variation of the ferrite magnetic moment against carbon concentration.

3.2   Magnetic properties of ferrite at low carbon concentration

3.2.1   Ferrite model

Because of the low carbon concentration in ISS, most magnetic calculations of ferrite can be done using the pure α-Fe model. During crystal growth, two components possess different lattice constants, and such lattice mismatch may result in residual stress, which may further affect the property of the magnetic material. In the quasi-ferrite, because of the role of the interstitial, a carbon atom may affect the position of body-centered Fe atom in the α-Fe. If the α-Fe lattice is the same as the two simple nesting cubic crystal lattices, then the displacement of the body-centered Fe atom induces lattice mismatch, and the mismatch strain can be determined with

$$\varepsilon = \frac{a_2 - a_1}{a_1}, \tag{15}$$

where ε is strain, a_1 is the original lattice parameter, Å, and a_2 is the mismatch lattice parameter, Å.

3.2.2   Band structure of α-Fe

Figure 3 shows the energy variation of main symmetric point R of 1st Brilliou zone of α-Fe against applied tension and compression load along [111] direction. The reason for proportional loading in that direction is to ensure the linear displacement produced between the nearest neighboring atoms in cell, while the angular displacement is not generated due to lacking the shear interaction. From the compression, the energy of the R-point is on the increase of load, which may be interpreted from the pair potential formed between two atoms. Contrary to the tension, there is a significant energy well for the energy change, and then the energy of the system is maintained constant substantially. If the lattice constant a=2.8664 Å of α-Fe was taken as the balanced position of the atom in cell, the curves shown in

Figure 3 could be converted to the curve shown in Figure 4. This means the analogous potential rule to comply with between two of the atoms, such as Lennard-Jones [14] and Morse [15].

By comparing the mismatch stress in the micro scale with the macro mechanical interaction in engineering, the ranges of compression and tension are reasonably less than 300 GPa. Figure 5 shows the band structure of compressive α-Fe between the loaded and the unloaded, while the band structure of tensile α-Fe is shown in Figure 6.

Due to the crystal field effect, for α-Fe, the 3d energy level can be split into five sublevels, in which the four sublevels on the top, $3d_{x^2-y^2}$, $3d_{z^2}$, $3d_{yz}$ and $3d_{xz}$, have higher energy state, while the sublevel $3d_{xy}$ at the bottom has lower energy state distribution in the first BZ. Therefore, from the analysis of the band width, we can conclude that the sublevels $3d_{x^2-y^2}$, $3d_{yz}$ and $3d_{xz}$ form metal compounds while the sublevel $3d_{xy}$ and level 3p then cannot form metal bonds. It can be interpreted by the atomic core state when the level energy is less than 3d. Otherwise,
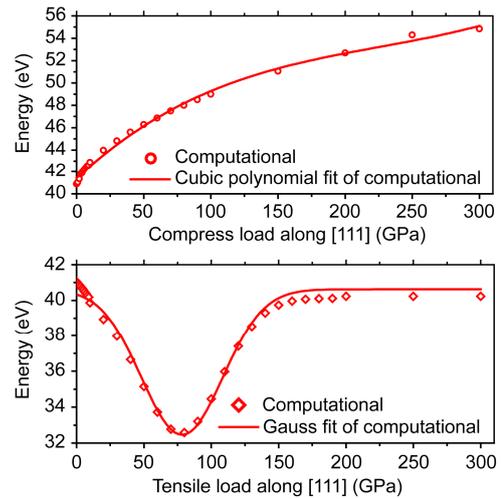

Figure 3   (Color online) Energy variation of main symmetric point R of 1st Brilliou zone against load.
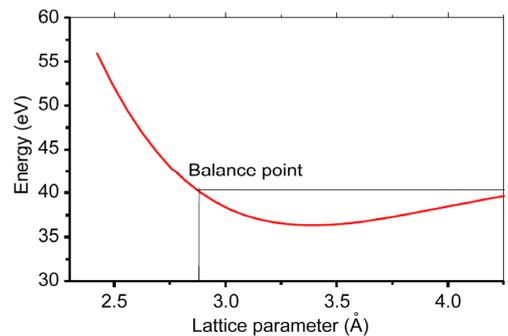
**Figure 4**   (Color online) Energy variation of main symmetric point R of 1st Brilliou zone against lattice parameter.

because the energy at 4s is lower than 3d, there is no bond for 4s (Figures 5 and 6). The energy levels involved in the formation of all metal compounds are unpaired electron orbital.

It can be seen under the given loading conditions that the energy at orbital 3d increases more apparently, because when the crystal is compressed, the ion core affects the external electron less, and the distance between the outer electrons decreases due to the compressive loading, resulting in the enhancement of electrostatic forces and the orbital energy, while the orbital energy of $3d_{yz}$, $3d_{xz}$ and 4s do not change the basic energy level. In contrast, in the interaction under tension, the ion core almost does not affect the external electron, and the distance between the outer electrons increases due to the external loading, resulting in a slight reduction of the electrostatic force and the 3d orbital energy, but the change in the orbital energy $3d_{yz}$, $3d_{xz}$ and 4s is insignificant (Figure 6), especially in the energy band below the Fermi surface.
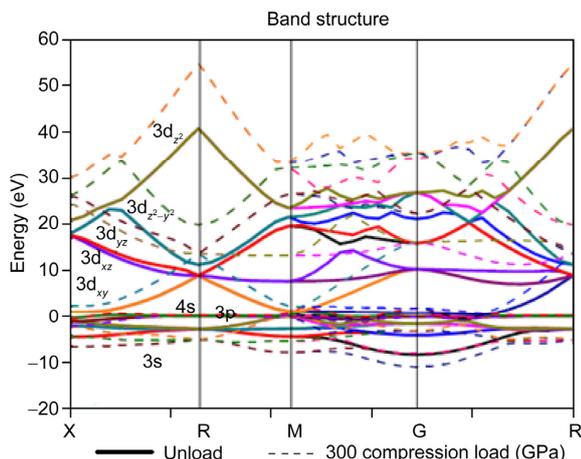
Figure 5 (Color online) Band structure comparison of [111] proportional loaded (compression) with unloaded.
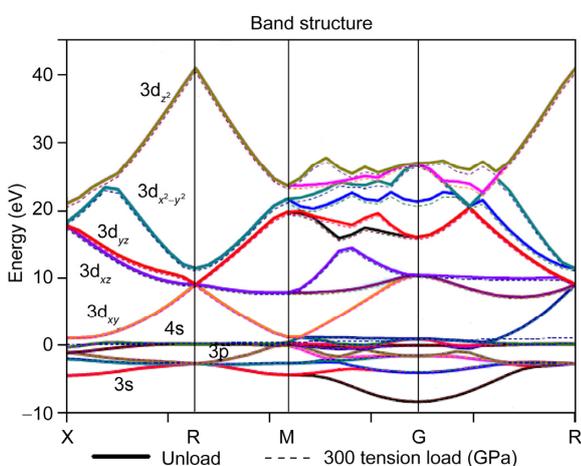
Figure 6 (Color online) Band structure comparison of [111] proportional loaded (tension) with unloaded.

It can be seen from Figure 5 that the band structure cannot be altered, but it increases in width under the mechanical loading in engineering. Since the width of the band depends on the interaction between the atoms, especially the nearest neighboring atoms, the stronger interaction induces the wider band.

3.2.3 Magnetic response of ferrite under proportioned [111] loaded

The magnetic moment of Fe atom in the free state (the ground state) is $6.7\mu_B$, while the magnetic moment of metal crystals α-Fe is $2.32\mu_B$, the experimental magnetic moment of iron in *bcc* crystal is $2.22\mu_B$, and the magnetic moment of the unloaded ferrite α-Fe obtained with the first-principles calculation is $2.24\mu_B$. It can be seen that the calculated magnetic moment of iron coincides with the experimental results [16]. Based on the SDFT and using the computational model mentioned above, the relationships between the magnetic change and the applied stress of α-Fe are shown in Figures 7 and 8, which show that: i) Under the given loading condition, the relationship between the magnetism and the applied stress is linear; ii) Under some load, the calculated magnet moment exhibits discontinuity. The intervals and the jumps of the discontinuities in the tension are almost identical with each other, and the similar tendency can also be observed in compression. This kind of continuities can be attributed to the lattice parameters changing with the increase of the applied load. For a given wave vector, when the conditions for the Bragg reflection are satisfied, the electrons will be reflected thoroughly and the corresponding energy state, as well as the corresponding magnetic moment, will no longer exist, which appears intermittently in the area. The linear relationships in Figure 7 are fitted with

$$M = \begin{cases} 2.1132+0.0026\sigma, & 0.00 < \sigma < 0.20, \\ 2.1139+0.0031\sigma, & 0.20 < \sigma < 0.65, \\ 2.1149+0.0027\sigma, & 0.65 < \sigma < 1.20. \end{cases} \quad (16)$$

The linear relationships in Figure 8 are fitted with

$$M = \begin{cases} 2.1132-0.0023\sigma, & 0.00 < \sigma < 0.30, \\ 2.1127-0.0026\sigma, & 0.30 < \sigma < 0.80, \\ 2.1128-0.0033\sigma, & 0.80 < \sigma < 1.35, \end{cases} \quad (17)$$

where M is the magnetic moment, and σ is the stress. This shows that the ferrite magnetic changes are associated with the loading mode. In tension loading, the enhanced electron spin polarized leads to magnetic moment increase. This can be interpreted at the micro level that the interaction length increases leading to the unpaired valence electron enhanced; On the contrary, in compression loading, the reducing electrons spin polarization leads to the magnetic moment decrease. Despite the scale effect, the fit relationship still explains the linear constitutive property of magnetism in the
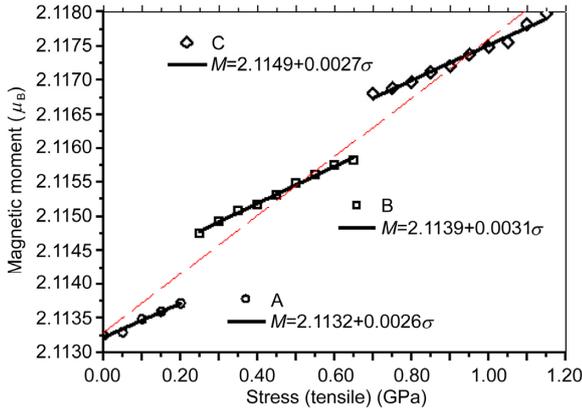
Figure 7   (Color online) Variation of the magnetic moment of α-Fe against applied tension stress.
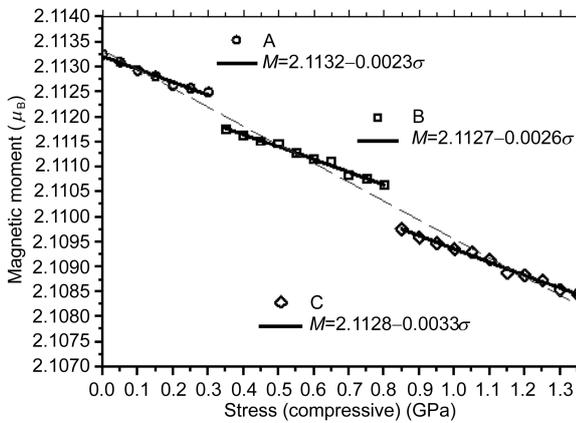
Figure 8   Variation of the magnetic moment of α-Fe against applied compression stress.

small strain state [5].

3.3   Variation of magnetism against lattice mismatch

Assuming that the C atom in the ISS lies in the position of face-centered [010], the calculated results suggest that the body-centered Fe in α-Fe deviates from its original equilibrium position in the direction (010) due to the interaction of interstitial C atom, but for the need of symmetry, C atoms are still in the face-centered [010] position, so the lattice parameters in the direction of (010) are changed. If we take the α-Fe crystal lattice as the same two simple nesting cubic crystal lattices, it is obvious that the displacement of the body-centered Fe atom will induce lattice mismatch, which conversely results in magnetic variance.

According to the results in sect. 3.2, the movement of the body-centered Fe atom in ferrite can be calculated with the following model: the constraint condition is that the lattice parameters in directions (100) and (001) keep constants for crystal periodicity, i.e., the lattice parameters of a and c keep constants, while b can be changed. The optimization of the geometric model and the differential charge distribution

are shown in Figure 9. Central C atom mainly forms Fe-C metal compounds with the nearest neighboring Fe atoms, and the lattice parameters in the directions (100) and (001) are reduced, but in the direction (010), driven by the interstitial C atom, the distance between the two body-centered Fe atoms in the neighboring cells increases evidently, so that the lattice parameter increases.

However, the lattice atoms suffer constraints increase with the increase of the superlattice layers due to the constraint of periodic boundary condition and interlayer exchange coupling between the layers [17–23], and finally the atoms move gradually to a normal lattice state. This accounts for constant lattice parameters a and c, and the change in b. Figure 9 shows the population analysis of the differential charge, and Figure 10 shows the relation between atomic layers and mismatch strain $\varepsilon_{(010)}$ in the direction of (010).

4   Conclusions

We draw the following conclusions by the calculation of the
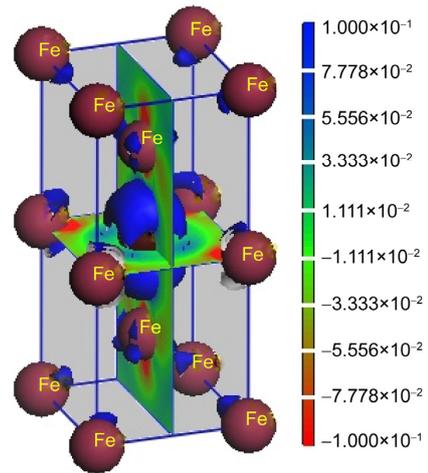
Figure 9   (Color online) Population analysis of the differential charge.
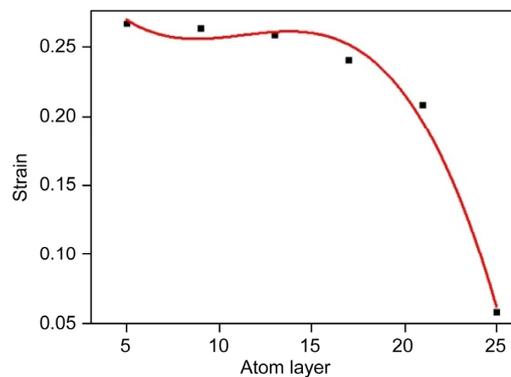
Figure 10   (Color online) Mismatch strain $\varepsilon_{(010)}$ against layers.

magnetic responses of ferrite super-lattice under constrained and unconstrained conditions.

1) The magnetism of ferrite increases with decreasing concentration of C atoms, and the magnetic properties of the ferrite is equivalent to the $1 \times 1 \times 1$ α-Fe cyclical cell when it satisfies the condition of $1 \times n \times 1$;
$$\lim_{n \to \infty}$$

2) Ferrite lattice mismatch generated due to the presence of crystalline periodicity constraints is mainly in the direction of (010), which is due to the existence of interstitial C atoms. The mismatch makes the large distance between the two of body-centered Fe atoms in the crystal for the relative repulsion, and at the same time, the atoms Fe and C form the corresponding Fe-C metal compounds in the same crystal plane. Under the condition of unconstraint, the lattice parameters decreasing in the directions of (100) and (001) induce the residual stress in the local area of ferrite;

3) The ferrite response of magnetism with stress in engineering is much smaller than the magnetic response due to lattice mismatch; it reflects the magnetic properties of ferrite in crystal structure. Because of the energy of core ion bellow 3d orbital cannot be changed under the condition of mechanical loading, and while the energy change above 3d orbital is smaller in microscope, there is less impact on the electron spin state, so the magnetic changes are smaller.

1   Doubov A A. Screening of weld quality using the metal magnetic memory effect. Weld World, 1998, 41(3): 196–199

2   Doubov A A. Study of metal properties using metal magnetic memory method. In: Proceedings of 7th European Conference on Non-destructive Testing. Copenhagen: NDTnet, 1998. 920–927

3   Doubov A A. A technique for monitoring the bends of boiler and steam-line tubes using the magnetic memory of metal. Therm Eng, 2001, 48(4): 289–295

4   Linnemann K, Klinkel S, Wagner W. A constitutive model for magnetostrictive and piezoelectric materials. Int J Solids Struct, 2009, 46: 1149–1166

5   Wan Y P, Fang D N, Hwang K C. Non-linear constitutive relations for magnetostrictive materials. Int J Nonlin Mech, 2003, 38: 1053–1065

6   Zhou H M, Zhou Y H, Zheng X J, et al. A general 3-D nonlinear magnetostrictive constitutive model for soft ferromagnetic materials. J Magn Magn Mater, 2009, 321: 281–290

7   Barth U V, Hedin L. A local exchange-correlation potential for the spin polarized case. J Phys C-Solid State Phys, 1972, 5: 1629–1642

8   Pant M M, Rajagopal A K. Theory of inhomogeneous magnetic electron gas. Solid State Commun, 1972, 10: 1157–1160

9   Levy M. Electron densities in search of Hamiltonians. Phys Rev A, 1982, 26(3): 1200–1208

10   Becke A D. Density-functional exchange-energy approximation with correct asymptotic-behavior. Phys Rev A, 1988, 38: 3098–3100

11   Perdew J P, Chevary J A, Vosko S H, et al. Atoms, molecules, solids, and surfaces: Applications of the generalized gradient approximation for exchange and correlation. Phys Chem B, 1992, 46: 6671–6687

12   Perdew J P, Burke K, Wang Y. Generalized gradient approximation for the exchange-correlation hole of a many-electron system. Phys Chem B, 1996, 54: 16533–16539

13   Perdew J P, Burke K, Ernzerhof M. Generalized gradient approximation made simple. Phys Rev Lett, 1996, 77(18): 3865–3868

14   Baskes M I. Many-body effects in *fcc* metals: A Lennard-Jones embedded-atom potential. Phys Rev Lett, 1999, 83(13): 2592–2595

15   Komanduri R, Chandrasekaran N, Raff L M. Molecular dynamics (MD) simulation of uniaxial tension of some single-crystal cubic metals at nanolevel. Int J Mech Sci, 2001, 43: 2237–2360

16   Rocker W, Kohlhaas R, Schöpgens H W. Magneto caloric effect and critical phenomena of iron, cobalt and nickel near the Curie temperature. J Phys, 1971, 32: 652–653

17   Hadj-Larbi A, Bouarab S. Magnetic profile and interlayer exchange coupling in *fcc* Fen/Nim (001) superlattices. Phys Rev B, 2002, 66: 144428–144435

18   Hadj-Larbi A, Adjaoud O, Bouarab S, et al. Magnetic map and interlayer exchange coupling in Fe/Ni (110) and Fe/Ni (111) superlattices. Surf Sci, 2005, 594: 148–155

19   Hadj-Larbi A, Ziane A, Bouarab S, et al. Effect on alloying at the Fe/Ni (001) interfaces on the interlayer exchange coupling. Eur Phys J B, 2006, 53: 29–34

20   Hong J S. Thickness-dependent magnetic anisotropy in ultrathin Fe/Co/Cu (001) films. Phys Rev B, 2006, 74: 172408–172411

21   Ziane A, Amitouche F, Hadj-Larbi A, et al. Relation between interlayer exchange coupling and nonferromagnetic behavior of Fe in Ni/Fe/Co superlattices. Phys Rev B, 2006, 73: 064411–064417

22   Le B O, Eriksson O, Johansson B. First-principles calculations of the magnetic anisotropy energy of Fe-V multilayers. Phys Rev B, 2002, 65: 134430–134438

23   Le B O, Pasturel A. First-principles determination of exchange interactions in delafossite $YCuO_{2.5}$. Phys Rev B, 2005, 71: 014432–014439